

A method for the microlensed flux variance of QSOs

Jeremy Goodman¹ and Ai-Lei Sun¹

¹*Department of Astrophysical Sciences, Princeton University, Princeton, NJ 08544, USA*

Drafted 2013 August 27.

ABSTRACT

A fast and practical method is described for calculating the microlensed flux variance of an arbitrary source by uncorrelated stars. The required inputs are the mean convergence and shear due to the smoothed potential of the lensing galaxy, the stellar mass function, and the absolute square of the Fourier transform of the surface brightness in the source plane. The mathematical approach follows previous authors but has been generalized, streamlined, and implemented in publicly available code. Examples of its application are given for Dexter and Agol’s inhomogeneous-disk models as well as the usual gaussian sources. Since the quantity calculated is a second moment of the magnification, it is only logarithmically sensitive to the sizes of very compact sources. However, for the inferred sizes of actual QSOs, it has some discriminatory power and may lend itself to simple statistical tests. At the very least, it should be useful for testing the convergence of microlensing simulations.

Key words: gravitational lensing; strong — accretion, accretion discs

1 INTRODUCTION

Gravitational microlensing by stars along the line of sight to a QSO is sensitive to the size and structure of the optically luminous regions of the accretion disk, which are otherwise unresolvable at present: sources of angular size much smaller than the Einstein ring of a lensing star can be strongly amplified, whereas more extended sources cannot be (e.g., Young 1981). Recent quasar surveys have turned up a number of quasars suitably aligned with intervening galaxies, and the analysis of their light curves has yielded two principal results. Firstly, in most cases the source size scales with wavelength approximately as expected for a steadily accreting, optically thick disk, namely $\theta \propto \lambda^{4/3}$ (Anguita et al. 2008; Eigenbrod et al. 2008; Poindexter et al. 2008; Bate et al. 2008; Mosquera et al. 2011; Muñoz et al. 2011; Mosquera et al. 2011; but Floyd et al. 2009 and Blackburne et al. 2011 find otherwise). Secondly however, the absolute source size is too large by at least half an order of magnitude (Pooley et al. 2007; Blackburne et al. 2011; Jiménez-Vicente et al. 2012). Not only is the source larger than thin-disk theory predicts for likely ranges of black-hole mass and accretion rate, but also, as Morgan et al. (2010) have emphasized, it is too large for any source that radiates locally as a black body unless the radial temperature profile is substantially shallower than $\theta^{-3/4}$.

If the latter conclusion is correct, then something is seriously wrong with steady-state thin-disk theory as applied to QSOs. The discrepancy is not small; stated in terms of the areas rather than the linear sizes of the sources, it is

more than an order of magnitude. Several physical possibilities would need to be explored, ranging from highly inhomogeneous disks (Dexter & Agol 2011), perhaps caused by thermal or viscous instabilities (Lightman & Eardley 1974; Syunyaev & Shakura 1975); to disk warps, perhaps driven by a radiation-pressure instability (Pringle 1996); to optically thick scattering-dominated winds; or even gap opening by embedded satellites (e.g., Armitage & Natarajan 2002; Goodman & Tan 2004). However, the error bars in the microlensing size estimates are still large; studies differ as to the magnitude of the size discrepancy, and sometimes even the sign (Rauch & Blandford 1991). The statistical methods used sometimes opaque, especially when entire photometric time series are fitted to simulations. For these among other reasons, one worries that the overlarge inferred sizes may be due to inadequate statistics or systematic errors. Ultimately this will be decided only by more data independently analyzed.

In the meantime, having no data of our own to offer, we revive and extend a semianalytic approach to the prediction of microlensing statistics pioneered by Deguchi & Watson (1987) and improved by Seitz & Schneider (1994), Seitz et al. (1994), and Neendorf (2003). The semianalytic method adds no noise to the comparison between models and data and avoids possible biases due to choices of numerical parameters, such as the numbers of rays shot or the size of the regions simulated in the lens and source plane. It is easily extended to the autocorrelation of the magnification as a function of time lag provided that the velocity dispersion of the lensing stars is small compared to the motion of the lensing galaxy across the line of

arXiv:1309.7369v1 [astro-ph.CO] 27 Sep 2013

sight. The method is limited, however, to second moments of the light curve. Simulations are more flexible and can address higher moments of the magnification and the structure of caustic crossings, effects that are more sensitive to the sizes of very compact sources. These are good scientific reasons to prefer simulations. Certain practical impediments to the use of the semianalytic method, however, are removable. The method is perceived to be cumbersome and hard to use, involving as it does multiple integrals and expansions in special functions. In the efficient but restricted version implemented by Neindorf (2003), it is limited to gaussian sources. In this paper, we develop an efficient and practical version of the semi-analytic formalism that can be applied to arbitrary source structures, not just gaussian ones. In hopes that it will be more widely used, we have implemented the method in Python code downloadable from a git repository <https://bitbucket.org/jjgoodman/mulensvar>.

The effort required by this method factors in a way well suited to exploring a large range of source structures and macrolensing parameters. The main part of the work is to calculate a kernel that depends upon dimensionless statistical properties of the lens such as optical depth, shear, and mean stellar mass or mass distribution. This kernel can be computed efficiently for almost any reasonable choice of these parameters, using a pre-computed special function (§3.1). The kernel so obtained is independent of the source structure. Second moments of magnification are obtained by convolving the kernel with the spatial autocorrelation function of the source. Hence if one is reasonably confident of the average properties of the lenses, then a single computed kernel may quickly be applied to many possible sources. Even if simulations are necessary, one can at least use this method as partial check on convergence with respect to the purely numerical parameters of the simulations, such as the number of rays, stars, and realizations. Although agreement with the semianalytic flux variance does not guarantee that the simulations are fully converged for all purposes, one should not trust simulations that do not show such agreement.

The plan of this paper is as follows. §2 introduces the lensing kernel and associated notation. §3 describes our algorithms for evaluating the lensing kernel numerically and (in certain limits) analytically. Most of this quite technical section can safely be skipped if one wishes to use our codes as they are, but one should read it carefully before attempting modifications. The asymptotic analytic results (21a) & (21b) and their physical interpretation may be of more general interest, however. Interpolation between these formulae captures much of the behavior of the microlensing kernel, as is demonstrated by Fig. 3. §4 presents numerical examples and tests. These include applications to Huchra’s Lens (Q2237+305) and to Dexter & Agol (2011)’s fragmented disks. The predictions of the method are compared with simulations made using a simple ray-shooting code. The agreement is satisfactory, but the convergence of the simulations to the predictions is somewhat slow with regard to domain size and number of stars: regions $\gtrsim 10^2\theta_E$ on a side are needed for 1% accuracy.

2 DEFINITIONS

Macrolensing by the large-scale mean potential of the intervening galaxy splits the source into macroimages separated typically by arcseconds. Microlensing by stars divides each macroimage into a cluster of subimages with angular separations comparable to the Einstein ring of a single star, $\theta_E = \sqrt{4GM_*D_{LS}/c^2D_S D_L}$, which is $\approx 2(M_*/M_\odot)^{1/2} \mu\text{as}$ ($\approx 10^{-11}$ rad) for typical lens and source redshifts $(z_L, z_S) = (0.5, 2.0)$. At the angular-diameter distance of the lens, this projects to $D_L\theta_E \sim 10^{-2}$ pc. In theoretical studies of microlensing, it is often necessary to consider a region several tens of θ_E across to allow for the interactions between caustics and for the motion of the line of sight across the lens plane (at, say, $0.03\theta_E \text{ yr}^{-1}$). Even so, the region of interest is scarcely larger than a parsec. On such scales the contribution of the large-scale smoothed galactic potential to the lens equation is well approximated by a locally constant linear transformation,

$$\mathbf{M} = \begin{pmatrix} 1 - \kappa - \gamma \cos 2\alpha & -\gamma \sin 2\alpha \\ -\gamma \sin 2\alpha & 1 - \kappa + \gamma \cos 2\alpha \end{pmatrix}. \quad (1)$$

The notation of Miralda-Escudé (1991) is used for the dimensionless convergence κ , total shear γ , and orientation α of the principal axes of the shear. The macrolensing magnification is $(\det \mathbf{M})^{-1} = [(1 - \kappa)^2 - \gamma^2]^{-1}$. The local mean surface density in stars contributes a portion κ_* to the convergence. The remainder, $\kappa' = \kappa - \kappa_*$, is due to dark matter and gas and is assumed to be smoothly distributed. Typically $\kappa_*/\kappa \sim 0.05 - 0.1$ (Mediavilla et al. 2009), but stars may dominate the convergence when the macroimage lies in the central parts of the lensing galaxy, as in Q2237+305.

Within a single macroimage, the lens equation relating a line of sight from Earth in direction $\boldsymbol{\theta}$ to its unlensed counterpart $\boldsymbol{\theta}_S$ on the source plane becomes

$$\boldsymbol{\theta}_S = \mathbf{M} \cdot \boldsymbol{\theta} + \left(\theta_E^2 \sum_k \frac{\boldsymbol{\xi}_k - \boldsymbol{\theta}}{|\boldsymbol{\xi}_k - \boldsymbol{\theta}|^2} + \kappa_* \boldsymbol{\theta} \right) \equiv \mathbf{M} \cdot \boldsymbol{\theta} + \boldsymbol{\phi}. \quad (2)$$

Here $\boldsymbol{\xi}_k$ is the angular position of the k^{th} microlensing star, with the origin of coordinates for $\boldsymbol{\theta}$ and $\boldsymbol{\xi}_k$ taken at the center of the macroimage. The term $\kappa_* \boldsymbol{\theta}$ has been grouped with the sum over stars to prevent double-counting the mean stellar convergence, since $-\kappa = -\kappa_* - \kappa'$ in \mathbf{M} . For the moment, all stars have the same mass and therefore the same θ_E^2 , but a mass function will be introduced later (§3.2). In the approximation that the sum above ranges over stars distributed throughout the lens plane with constant mean number per unit area, the net stellar deflection $\boldsymbol{\phi}$ is a random variable with zero mean and stationary statistics. In other words, the joint probability density for this variable to take on values $\{\boldsymbol{\phi}_1, \dots, \boldsymbol{\phi}_n\}$ at positions $\{\boldsymbol{\theta}_1, \dots, \boldsymbol{\theta}_n\}$ depends upon the differences $\boldsymbol{\theta}_i - \boldsymbol{\theta}_j$ but not on the centroid $\bar{\boldsymbol{\theta}} = (\boldsymbol{\theta}_1 + \dots + \boldsymbol{\theta}_n)/n$. Binary and higher-multiplicity correlations among the stars would not be incompatible with stationary statistics but would make results along the lines of this paper almost impossible. Such correlations could be represented in simulations quite easily but rarely are.

An explicit expression is possible for Fourier transform $P(\boldsymbol{\omega}_1, \dots, \boldsymbol{\omega}_n)$ of the n -point probability density

$P(\phi_1, \dots, \phi_n)$. We call this the ‘‘characteristic function.’’

$$\begin{aligned} & \langle \exp[i\omega_1 \cdot \phi(\theta_1) + \dots + i\omega_n \cdot \phi(\theta_n)] \rangle = \\ & \exp \left\{ \nu \int \left[\exp \left(i \sum_{j=1}^n \frac{\theta_E^2 \omega_j \cdot (\xi - \theta_j)}{|\xi - \theta_j|^2} \right) \right. \right. \\ & \left. \left. - 1 - i \sum_{j=1}^n \frac{\theta_E^2 \omega_j \cdot (\xi - \theta_j)}{|\xi - \theta_j|^2} \right] d^2 \xi \right\}. \quad (3) \end{aligned}$$

Here $\langle \dots \rangle$ denotes expectation value, and $\nu \equiv \kappa_*/\pi\theta_E^2$ is the mean number of stars per unit area. Chandrasekhar (1943) derived this for $n = 1$, and Deguchi & Watson (1987) stated the result for $n = 2$ without derivation. Seitz & Schneider (1994) devote an entire paper to the discussion of the 2-point function and its inverse Fourier transform. For completeness, we sketch a derivation here for general n : Consider the counterpart to the left side of eq. (3) when ϕ_j replaced by $\phi'_j \equiv \phi_j - \kappa_*\theta_j$. The primed variables do not have stationary statistics because their means are $-\kappa_*\theta_j$. However, the contribution of a small area A of the lens plane with centroid ξ_A to their characteristic function is, with $f_A \equiv \sum_j \theta_E^2 \omega_j \cdot (\xi_A - \theta_j)/|\xi_A - \theta_j|^2$,

$$\sum_{N_A=0}^{\infty} \frac{(\nu A)^{N_A}}{N_A!} e^{-\nu A} e^{iN_A f_A} = \exp \left[\left(e^{i f_A} - 1 \right) \nu A \right],$$

if the number of stars within area A (N_A) is Poissonian with mean νA . Multiplying the independent contributions from all such areas in the lens plane gives eq. (3) except for the final term within the square brackets, which can be explained as follows: If the stars were restricted to a circular region $|\xi| < R$, then the average deflection due to these stars at $|\theta_j| < R$ would be

$$\nu \theta_E^2 \int \frac{\xi - \theta_j}{|\xi - \theta_j|^2} d^2 \xi = -\kappa_* \theta_j.$$

Thus the term in question removes the mean deflection from the characteristic function, as appropriate for the ϕ_j rather than the ϕ'_j .

2.1 Moments of the flux

For a transparent lens, the observed surface brightness I in direction θ is equal to the unlensed surface brightness I_0 at the position $\theta_S = \mathbf{M} \cdot \theta + \phi(\theta)$ where the lensed ray intercepts the source plane. Therefore, the flux of a macroimage summed over all of its microimages is

$$F = \int I(\theta) d^2 \theta = \int I_0(\mathbf{M} \cdot \theta + \phi) d^2 \theta,$$

The source and lensing variables can be separated by introducing the Fourier transform \hat{I}_0 of the unlensed source,

$$I_0(\theta) = \int \frac{d^2 \omega}{(2\pi)^2} \hat{I}_0(\omega) e^{i\omega \cdot \theta}, \quad (4)$$

so that

$$F = \int \frac{d^2 \omega}{(2\pi)^2} \hat{I}_0(\omega) \int d^2 \theta e^{i\omega \cdot (\mathbf{M} \cdot \theta + \phi)}. \quad (5)$$

The n^{th} moment of the flux is therefore

$$\begin{aligned} \langle F^n \rangle &= \left[\prod_{j=1}^n \int \frac{d^2 \omega_j}{(2\pi)^2} \hat{I}_0(\omega) \int d^2 \theta_j e^{i\omega_j \cdot \mathbf{M} \cdot \theta_j} \right] \\ &\times \langle \exp[i\omega_1 \cdot \phi(\theta_1) + \dots + i\omega_n \cdot \phi(\theta_n)] \rangle. \end{aligned}$$

The expectation value $\langle \dots \rangle$ is independent of the centroid $\bar{\theta} \equiv (\theta_1 + \dots + \theta_n)/n$. This can be used to reduce the number of vectorial integrations by two. Setting $\theta_j = \theta'_j + \bar{\theta}$ and integrating over $\bar{\theta}$ produces (dropping the primes hereafter)

$$\begin{aligned} \langle F^n \rangle &= (\det \mathbf{M})^{-1} \left[\prod_{j=1}^n \int \frac{d^2 \omega_j}{(2\pi)^2} \hat{I}_0(\omega) \int d^2 \theta_j e^{i\omega_j \cdot \mathbf{M} \cdot \theta_j} \right] \\ &\times (2\pi n)^2 \delta^2(\omega_1 + \dots + \omega_n) \delta^2(\theta_1 + \dots + \theta_n) \\ &\times \langle \exp[i\omega_1 \cdot \phi(\theta_1) + \dots + i\omega_n \cdot \phi(\theta_n)] \rangle. \quad (6) \end{aligned}$$

For $n = 1$, the delta functions absorb both integrations, so that $\langle F \rangle \rightarrow (\det \mathbf{M})^{-1} \hat{I}_0(\mathbf{0})$, which is the correct expression for the mean macrolensed flux.

As in previous works, our numerical methods are limited to the lowest nontrivial moment, $n = 2$. We set $\omega_1 = -\omega_2 \equiv \omega$ and $\theta_2 = -\theta_1 = \Delta\theta/2$. Then

$$\langle F^2 \rangle = (\det \mathbf{M})^{-2} \int \frac{d^2 \omega}{(2\pi)^2} |\hat{I}_0(\omega)|^2 \hat{J}(\omega), \quad (7)$$

$$\hat{J}(\omega) = \det \mathbf{M} \int d^2 \Delta\theta e^{i\omega \cdot \mathbf{M} \cdot \Delta\theta} \langle e^{i\omega \cdot [\phi(\theta) - \phi(\Delta\theta)]} \rangle. \quad (8)$$

Once the kernel $\hat{J}(\omega)$ has been calculated, equation (7) can be used to find the second moment of the flux for a general source structure with spatial power spectrum $|\hat{I}_0(\omega)|^2$. Furthermore, if one adopts the ‘‘frozen-screen’’ approximation in which the motions of the stars within the lensing galaxy are neglected compared to the transverse motion \mathbf{V}_\perp of the lensing galaxy across the line of sight, then one can use the same kernel to calculate the correlation between the microlensed flux at finite time lag:

$$\begin{aligned} \langle F(t)F(t+\tau) \rangle &\approx (\det \mathbf{M})^{-2} \\ &\times \int \frac{d^2 \omega}{(2\pi)^2} |\hat{I}_0(\omega)|^2 \hat{J}(\omega) \exp \left(\frac{i\omega \cdot \mathbf{V}_\perp \tau}{D_L} \right). \end{aligned} \quad (9)$$

As discussed by Kundic & Wambsganss (1993), however, the frozen-screen approximation is not very accurate, especially at high optical depth (Wyithe et al. 2000).

As discussed in §3.3, $\hat{J}(\omega)$ contains a term proportional to $\delta^2(\omega)$ that accounts for the square of the mean flux in eqs. (7) & (9). If this term is subtracted from $\hat{J}(\omega)$, the right sides of these equations yield the variance and covariance of the flux. In other words, subtracting the delta function from $\hat{J}(\omega)$ has the same effect as removing the mean from F before its second moments are calculated. The numerical method that we use to evaluate $\hat{J}(\omega)$ makes this subtraction automatic. At the risk of confusion, *we hereafter interpret $\hat{J}(\omega)$ as the modified kernel so that $\langle F^2 \rangle \rightarrow \text{var}(F)$ in eq. (7).*

2.2 Transformation and scaling of the characteristic function

In the approach outlined above, the first step toward $\langle F^n \rangle$ is to calculate the characteristic function (3). This involves integration over the vector ξ . The result will evidently be a function of the $2n$ vector-valued parameters $(\omega_1, \dots, \omega_n)$ and $(\theta_1, \dots, \theta_n)$. Because of the two delta functions in eq. (6), only $2n - 2$ of these parameters are independent, equivalent to $4n - 4$ independent scalar parameters. Because the characteristic function is independent of the macrolensing shear, it is statistically isotropic and hence unaffected

by an overall rotation of the lens plane. This reduces the number of essential scalar parameters by one. The following scaling property reduces the number by one more. Let $\omega_j \rightarrow \sigma \omega_j$, $\theta_j \rightarrow \sigma \theta_j$, with the same factor σ for all j . Rescaling the dummy integration variable $\xi \rightarrow \sigma \xi$ and the stellar number density $\nu \rightarrow \sigma^{-2} \nu$ [equivalently $\theta_E^2 \rightarrow \sigma^{-2} \theta_E^2$ or $\kappa_* \rightarrow \sigma^{-2} \kappa_*$] restores the integration to its form for $\sigma = 1$.

As a result, the number of essential scalar parameters needed to specify the n -point characteristic function is $4n - 6$. (This assumes $n > 1$, else the characteristic function collapses to a constant.) For $n = 2$, this is manageable. The logarithm of the two-point characteristic function can be tabulated for a grid of values of two parameters, each entry in the table requiring a two-dimensional quadrature. Fortunately the calculation need be done only once, since it is independent of the macrolensing matrix (\mathbf{M}), and even the dependence on ν and θ_E^2 (equivalently, $\kappa_* = \pi \nu \theta_E^2$) can be scaled out. This table can then be used to calculate $\text{var}(F)$ for any combination of macrolensing, stellar density, and source structure.

Before going into those details, we generalize a change of variables introduced by Neindorf (2003). Associate with each real-valued vector $\mathbf{v} = (v_x, v_y)$ a complex number $\tilde{v} = v_x + iv_y$. The argument of the inner exponential of eq. (3) becomes if_x in terms of the meromorphic function

$$\tilde{f}(\tilde{\xi}) \equiv \theta_E^2 \sum_{j=1}^n \frac{\tilde{\omega}_j}{\tilde{\xi} - \tilde{\theta}_j}. \quad (10)$$

The change of variables $\tilde{\xi} \rightarrow \tilde{f}$ has jacobian $|d\tilde{f}/d\tilde{\xi}|^{-2}$, so that the integral in eq. (3) becomes

$$\nu \iint \left(e^{if_x} - 1 - if_x \right) \left| d\tilde{\xi}/d\tilde{f} \right|^2 df_x df_y. \quad (11)$$

The derivative $d\tilde{\xi}/d\tilde{f}$ is needed as a function of \tilde{f} , which requires inverting the function (10). This leads to a polynomial of degree n in $\tilde{\xi}$. The jacobian must be summed over all n roots. A slight simplification is that the coefficient of $\tilde{\xi}^{n-1}$ in the polynomial vanishes because $\sum_j \tilde{\omega}_j = \sum_j \tilde{\theta}_j = 0$, so that the n roots for $\tilde{\xi}$ sum to zero.

In particular, for $n = 2$ the roots are

$$\tilde{\xi} = \pm \sqrt{\tilde{\theta}_1(\tilde{\theta}_1 + 2\theta_E^2 \tilde{\omega}_1 / \tilde{f})}.$$

Set $\omega = \omega_1 = -\omega_2$ and $\Delta\theta = 2\theta_2 = -2\theta_1$. Rescale the integration variable to $\tilde{r} \equiv u - iv \equiv \tilde{f} \Delta\tilde{\theta} / 4\theta_E^2 \tilde{\omega}$. Finally, let ψ be the angle between ω and $\Delta\theta$, and $\Delta\theta \equiv |\Delta\theta|$. The 2-point function is then

$$\left\langle e^{i\omega \cdot [\phi(0) - \phi(\Delta\theta)]} \right\rangle = \exp \left[\frac{\kappa_*(\Delta\theta)^2}{4\pi\theta_E^2} H \left(\frac{4\theta_E^2}{\Delta\theta} \omega \right) \right], \quad (12a)$$

where H as a function of $\beta \Leftrightarrow (\beta \cos \psi, \beta \sin \psi)$ is

$$H(\beta) \Leftrightarrow H(\beta, \psi) \equiv \iint \frac{\exp[i\beta(u \cos \psi + v \sin \psi)] - 1 - i\beta(u \cos \psi + v \sin \psi)}{2(u^2 + v^2)^{3/2} \sqrt{(u-1)^2 + v^2}} dudv. \quad (12b)$$

3 NUMERICAL EVALUATION

Here we describe the methods used to compute the kernel $\hat{J}(\omega)$ for the second moment of the flux [eq. (8)]. The first

step is to compute and tabulate the function $H(\beta)$ (§3.1). It is quite easy to incorporate a distribution of stellar masses at this stage (§3.2). The final step is to carry out the integration over $\Delta\theta$ in eq. (8), which is really a double integral since $\Delta\theta$ is a 2-component vector (§3.3). As a check on the numerics, we derive asymptotic results for $\omega\theta_E \ll 1$ and $\omega\theta_E \gg 1$ and interpret these results physically (§3.4).

3.1 The function H

Since u and v in eq. (12b) are actually scaled versions of the ‘‘force’’ (10), the singularity of the integrand at the origin represents the large area available to distant stars that exert weak deflections. Without the subtracted terms in the numerator, eq. (12b) would be a two-dimensional Fourier transform. But without at least the -1 , the singularity at the origin would not be integrable. We considered softening the singularities so that we could separate the three terms in the numerator and evaluate the first by 2D FFTs. But instead, like Seitz & Schneider (1994), we chose to expand $H(\beta, \psi)$ as a Fourier series in ψ :

$$\begin{aligned} H(\beta, \psi) &= \frac{1}{2}\pi \int_0^\infty \frac{dr}{r^2} [J_0(\beta r) - 1] b_{1/2}^{(0)}(r) \\ &\quad + i\pi(\cos \psi) \int_0^\infty \frac{dr}{r^2} [J_1(\beta r) - \frac{1}{2}\beta r] b_{1/2}^{(1)}(r) \\ &\quad + \pi \sum_{n=2}^\infty i^n \cos(n\psi) \int_0^\infty \frac{dr}{r^2} J_n(\beta r) b_{1/2}^{(n)}(r) \\ &\equiv \sum_{n=0}^\infty i^n h_n(\beta) \cos(n\psi). \end{aligned} \quad (13)$$

This representation has two advantages: (i) H is dominated by the terms for $n \leq 2$ at both large and small β ; (ii) convolution with a stellar mass spectrum, as described below, acts in the radial direction, i.e. along lines of constant polar angle ψ . The Bessel functions, J_n , result from expanding the exponential in (12b) as a Fourier series in $\psi - \alpha$, where $\alpha = \tan^{-1}(v/u)$. The Laplace coefficients (e.g., Brouwer & Clemence 1961)

$$b_{1/2}^{(n)}(r) \equiv \frac{1}{\pi} \int_0^{2\pi} \frac{\cos n\phi d\phi}{\sqrt{1+r^2-2r\cos\phi}} = \frac{2}{\pi\sqrt{r}} Q_{n-1/2} \left(\frac{1+r^2}{2r} \right), \quad (14)$$

result from expanding the second part of the denominator of eq. (12b). Here $Q_{n-1/2}$ are Legendre functions of the second kind and are calculated in our code by recursion on n starting from expressions for $Q_{-1/2}$ and $Q_{+1/2}$ in terms of complete elliptic integrals, or by hypergeometric series. The radial integrals are performed numerically in the complex r plane with due attention to the branch points at $r = 1$.

To facilitate convolution with a stellar mass function, it is convenient to tabulate the functions $h_n(\beta)$ on a grid uniformly spaced in $\ln \beta$. We typically use $\Delta \ln \beta = 0.01$ in the range $10^{-3} \leq \beta \leq 10^2$. The first three functions $h_0 \dots h_2$ dominate the series, though convergence with respect to n is slow at $\beta \sim 1$. We usually tabulate up to $n_{\text{max}} = 7$, tapering the series to hasten convergence. These choices are input parameters to our code. The functions $h_n(\beta)$ with $n \geq 2$

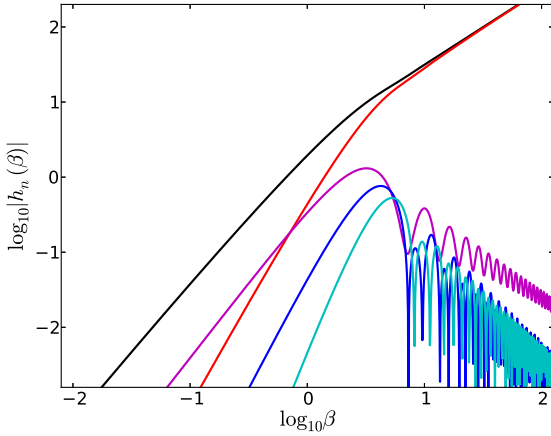


Figure 1. The first few azimuthal harmonics $h_n(\beta)$ of the function $H(\beta)$ determining the 2-point characteristic function [eqs. (12b) & (13)]. From top to bottom at $\beta = 1$, these are $n = 0, 1, 2, 3, 4$.

oscillate in β with period $\approx 2\pi$; this is due to logarithmic singularities of the Laplace coefficients at $r = 1$. In order to resolve these oscillations on a logarithmic grid, it is necessary that $\beta_{\max}\Delta \ln \beta < \pi$.

For extrapolation in β beyond the range of the table,

$$H(\beta, \psi) \rightarrow \frac{\pi}{4}\beta^2(\ln \beta + C_0) - \frac{\pi}{8}\beta^2 \cos 2\psi + O(\beta^3 \ln \beta),$$

as $\beta \rightarrow 0$;

$$H(\beta, \psi) \rightarrow -\pi\beta - i\pi(\beta - 1) \cos \psi + O(\beta^{-1}),$$

as $\beta \rightarrow \infty$. (15)

The constant $C_0 = \gamma - 1 - \ln 8 \approx -2.5022$.

3.2 Incorporating a stellar mass spectrum

The stellar mass (M_*) enters the problem through the square of the Einstein-ring radius, $\theta_E^2 \propto M_*$, in equation (3) for the n -point characteristic function. This makes it easy to introduce a spectrum of stellar masses. Let $f(\log M_*)d \log M_*$ represent the fraction of the total number of stars that have masses in the logarithmic interval $d \log M_*$. (Here $\log \equiv \log_{10}$.) The mean mass is then

$$\overline{M_*} = \int_{-\infty}^{\infty} M_* f(\log M_*) d \log M_*.$$

Let θ_E be the Einstein-ring radius based on the mean mass, $\theta_E^2 \equiv 4G\overline{M_*}D_{LS}/c^2D_LD_S$. To represent the mass spectrum $f(\log M_*)$ in the 2-point function $H(\beta)$, one need only make the replacements by the replacement

$$h_n(\beta) \rightarrow \bar{h}_n(\beta) = \int_{-\infty}^{\infty} h_n(10^x \beta) f(x) dx. \quad (16)$$

in the polar expansion (13). The asymptotics (15) need to be adjusted accordingly.

In fact, provided $f(x)$ itself is reasonably smooth, integrating over a mass spectrum would accelerate the convergence of the radial integrals in (13), because

$\int J_n(10^x \beta r) f(x) dx$ decays exponentially rather than oscillates when $\log(\beta r)$ is larger than the width of $f(x)$. This would allow us to integrate entirely on the real r axis. However, we choose to tabulate the h_n for a single mass. The smoothing (16) is performed very easily after the fact with any desired mass function. We adopt the log-normal form

$$f(\log M_*) = \frac{1}{\sqrt{2\pi}\sigma^2} \exp[-(\log M - \log M_c)^2/2\sigma^2]. \quad (17)$$

The replacement (16) should leave the mean mass unchanged; this requires that the characteristic mass $M_c = \overline{M_*} \exp[-(\sigma \ln 10)^2/2]$. In our code, by default, $\sigma = 0.3$ in agreement with the initial mass function recommended by Chabrier (2003) for the spheroidal component of the Galaxy [$\sigma = 0.33 \pm 0.03$, $M_c = 0.22 \pm 0.05 M_\odot$], except that Chabrier replaces the tail of the log-normal function above $0.7 M_\odot$ with a power law of roughly Salpeter slope ($x = 1.3$). The assumption is that since the spheroid is an old population, most of the stars in the tail will have evolved off the main sequence, effectively truncating the present-day mass function at the turnoff ($0.7 M_\odot$). Our code omits this refinement and uses the log-normal form without truncation.

3.3 The outer integral

Given the function $H(\beta)$, it remains to compute

$$\hat{J}(\omega) = \det \mathbf{M} \int d^2 \Delta \theta e^{-i\Delta \theta \cdot \mathbf{M} \cdot \omega} \exp \left[\frac{\kappa_* \Delta \theta^2}{4\pi \theta_E^2} H \left(\frac{4\theta_E^2 \omega}{\Delta \theta} \right) \right]. \quad (18)$$

As written, however, this double integral is not convergent for small ω and large $\Delta \theta$. Following (15), $H(\beta) \propto \beta^2 \ln \beta$ as $\beta \rightarrow 0$, whence the second exponential above tends to unity as $\omega \theta_E \rightarrow 0$. The rest of the integrand oscillates with constant modulus, whence $\hat{J}(\omega) \rightarrow (2\pi)^2 \delta^2(\omega)$ as $\omega \rightarrow 0$.

This is to be expected. A very extended source will have a Fourier transform $\hat{I}_0(\omega)$ that decreases rapidly with increasing $|\omega|$. Such a source should suffer little microlensing, so that $\langle F^2 \rangle = \langle F \rangle^2$. But the mean macrolensed flux is $\langle F \rangle = (\det \mathbf{M})^{-1} \hat{I}_0(\mathbf{0})$. Comparison with eq. (8), shows that the microlensing kernel must contain exactly the delta function identified in the previous paragraph.

For numerical purposes one must have a convergent expression. One option is to subtract unity from the second exponential in eq. (18). This removes the problem at small ω but creates a similar problem at large ω . A better tactic is to multiply the integrand by a broad and smooth window function that gradually tapers to zero at large $\Delta \theta$; this smears the delta function into a narrow but finite spike centered at ω without much changing the finite part of the integral at $\omega > 0$. Instead, we have chosen to evaluate eq. (18) by a version of Euler summation, which works as follows (e.g. Hardy 1949). Let $\sum_k (-1)^k a_k$ be an alternating series in which the terms $\{a_k\}$ have constant sign but may increase, provided $\lim_{k \rightarrow \infty} (a_{k+1}/a_k) = 1$. Let $S_n^{(0)} = \sum_{k=0}^{n-1} (-1)^k a_k$ be the n^{th} partial sum, and for $m > 0$

$$S_n^{(m)} = \frac{1}{2} \left[S_n^{(m-1)} + S_{n+1}^{(m-1)} \right] = 2^{-m} \sum_{j=0}^m \binom{m}{j} S_{n+j}^{(0)}.$$

If the sequence $\{S_n^{(0)}\}$ converges, then $\{S_n^{(m)}\}$ converges to the same limit. But $\{S_n^{(m)}\}$ may converge when $\{S_n^{(0)}\}$ does

not. For example, if $a_k = k$ then $\{S_n^{(m)}\} \rightarrow -1/4$ for $m \geq 2$, which is the “correct” result if this series is regarded as the limit of $\sum_k k(-x)^k = x(d/dx)(1+x)^{-1}$ as $x \rightarrow 1^-$.

To apply this, we set $(-1)^k a_k$ equal to the integral (18) restricted to the annulus

$$k \frac{\pi}{\mu} \leq |\Delta\theta| \leq k \frac{\pi}{\mu}, \quad \text{where } \mu \equiv |\mathbf{M} \cdot \boldsymbol{\omega}|.$$

For sufficiently large k ,

$$(-1)^k a_k \sim 2\pi \det \mathbf{M} \int_{k\pi/\mu}^{(k+1)\pi/\mu} d\Delta\theta J_0(\mu\Delta\theta) (\Delta\theta)^{1-\kappa_*\theta_E^2\omega^2}$$

The Bessel function $J_0(z) \sim \sqrt{2/\pi z} \cos(z - \pi/4)$ for $z \gg 1$. Hence $a_k \sim k^\sigma$ with $\sigma = 1/2 - \kappa_*\theta_E^2\omega^2$. After inspecting the smoothed partial sums $S_n^{(m)}$ for residual oscillations, our code adds more annuli as needed to enable further smoothing. This works reasonably well and automatically discards the delta function at $\boldsymbol{\omega} = 0$.

3.4 Limiting behaviors of the kernel and their interpretation

We can check the numerical results against analytical ones for $\omega\theta_E \ll 1$ and for $\omega\theta_E \gg 1$. Let ω be small enough so that it makes sense to replace the second exponential in (18) by the first two terms of its power series. Discard the leading term (unity), which gives the delta function. Also ignore the small contribution from the range $0 \leq \Delta\theta \lesssim 4\theta_E^2\omega$, so that $H(\beta)$ may be replaced by the top line of eq. (15). After integration over the azimuth of $\Delta\theta$,

$$\begin{aligned} \hat{J}(\boldsymbol{\omega}) &\approx 2\pi\kappa_*(\omega\theta_E)^2 \det \mathbf{M} \int_0^\infty d\Delta\theta \\ &\times \Delta\theta \left[\ln \left(\frac{4\theta_E^2\omega}{\Delta\theta} \right) J_0(\mu\Delta\theta) + \frac{1}{2} J_2(\mu\Delta\theta) \cos 2\alpha \right], \end{aligned} \quad (19)$$

where α is the angle between $\boldsymbol{\omega}$ and $\boldsymbol{\mu} \equiv \mathbf{M} \cdot \boldsymbol{\omega}$. The standard integral (Abramowitz & Stegun 1970, §11.4.16)

$$\int_0^\infty t^\mu J_\nu(t) dt = 2^\mu \frac{\Gamma(\frac{\nu+\mu+1}{2})}{\Gamma(\frac{\nu-\mu+1}{2})}. \quad (20)$$

converges only if $\mu + \nu > -1$ and $\mu < \frac{1}{2}$ but can be analytically continued via the right side where that is finite and nonzero. Logarithms can be inserted by differentiation with respect to μ . In particular,

$$\int_0^\infty dt J_0(t) t \ln t \rightarrow -1, \quad \int_0^\infty dt J_2(t) t \rightarrow +2.$$

Applying these rules to eq. (19) yields

$$\hat{J}(\boldsymbol{\omega}) \approx 4\pi\kappa_*\theta_E^2 \det \mathbf{M} \frac{(\boldsymbol{\omega} \cdot \mathbf{M} \cdot \boldsymbol{\omega})^2}{|\mathbf{M} \cdot \boldsymbol{\omega}|^4}, \quad 0 < \omega\theta_E \ll 1. \quad (21a)$$

On the other hand, when $\omega\theta_E \gg 1$, we may approximate H by the second line of eq. (15), with the result

$$\hat{J}(\boldsymbol{\omega}) \approx 2\pi \det \mathbf{M} \frac{\kappa_*\omega}{(\kappa_*^2\omega^2 + |\mathbf{M}' \cdot \boldsymbol{\omega}|^2)^{3/2}} \quad \text{if } \omega\theta_E \gg 1. \quad (21b)$$

Here $\mathbf{M}' \equiv \mathbf{M} + \kappa_*\mathbf{1}$, i.e. the residual of the macrolensing matrix when the mean stellar convergence is removed.

For a spectrum of stellar masses, eq. (21b) is unchanged, but eq. (21a) is multiplied by $\overline{M_*^2}/\overline{M_*}^2$ if θ_E^2 is based on the

mean mass $\overline{M_*}$. For a log-normal mass function with dispersion σ in $\log M_*$, the correction factor is $\exp[(\sigma \ln 10)^2]$.

3.4.1 Physical interpretation

The Fourier transform $\hat{I}_0(\boldsymbol{\omega})$ of a compact source has significant power at large values of its argument, $\boldsymbol{\omega}$. Therefore, the variance of the microlensed flux from such a source should be dominated by the asymptotic behavior (21b), which scales with $|\boldsymbol{\omega}|$ as ω^{-2} . Suppose that the spatial power spectrum $|\hat{I}_0(\boldsymbol{\omega})|^2 \sim \text{constant} \equiv C$ for $\omega < \Theta_S^{-1} \equiv \omega_S$, where Θ_S is the angular size of the source, and that the power spectrum falls off rapidly for $\omega > \omega_S$. Then if $\omega_S \gg \theta_E^{-1}$, it follows from eq. (21b) that $\text{var}(F)/\langle F \rangle^2 \propto C \log \omega_S$, with a constant of proportionality that depends upon κ_* , $\det \mathbf{M}$, and the angular dependence of $|\mathbf{M}' \cdot \boldsymbol{\omega}|$. Hence the flux variance diverges logarithmically in the limit that the angular size of the source tends to zero, as expected.

In the opposite limit of an extended source, $\Theta_S \gg \theta_E$, similar reasoning based on the small- ω asymptotics (21a) leads to $\text{var}(F)/F_0^2 \propto \omega_S^2 \propto \Theta_S^{-2}$. Why should sources larger than the Einstein ring of an individual star show any microlensing fluctuations at all? The answer is that the stellar convergence, whose average value we denote by κ_* , is subject to Poisson fluctuations in the number of stars projected onto the source:

$$\frac{\Delta\kappa_*}{\kappa_*} \sim \frac{\Delta N_*}{N_*} \sim N_*^{-1/2} \sim (\pi\omega\Theta_S^2)^{-1/2}.$$

Small fluctuations in the convergence translate linearly to fluctuations in magnification, whose variance (normalized by the mean magnification) therefore scales as Θ_S^{-2} .

4 NUMERICAL EXAMPLES AND APPLICATIONS

The poster child of microlensed quasars is Q2237+305, variously known as Huchra’s Lens after its discoverer, or the Einstein Cross. For the brightest of the four visible macroimages, Poindexter & Kochanek (2010) estimate that κ , κ_* , and γ are all close to 0.4. Hence the stars dominate the convergence, and the mean magnification of this image is $[(1 - \kappa - \gamma)(1 - \kappa + \gamma)]^{-1} \approx 5$.

Figure 2 shows the microlensing kernel numerically computed for these parameters. The anisotropy of the kernel—its dependence upon the angle α describing the direction of $\boldsymbol{\omega}$ —is due to the anisotropy of the macrolensing matrix, \mathbf{M} . The symmetries of the kernel are such that it suffices to calculate $\hat{J}(\boldsymbol{\omega})$ for $0 \leq \alpha \leq \pi/2$, where α is measured with respect to the eigenvector of \mathbf{M} corresponding to the eigenvalue of smaller absolute value.

The logarithmic axes influence the visibility of some details. There are small-amplitude wiggles in the curves in the decade $1 < \omega\theta_E < 10$ at the level of tens of percents, somewhat more pronounced for smaller magnifications. These are vestiges of much stronger oscillations in the azimuthal harmonics of the H function [Fig. 1]. The curves in Fig. 2 for different α are farther apart near $\omega = 0$ than as $\omega \rightarrow \infty$. This shows that $\hat{J}(\boldsymbol{\omega}) = \hat{J}(\omega \cos \alpha, \omega \sin \alpha)$ is not separable in ω and α . Although we do not show it here, the inseparability is yet more striking for the more typical case that $\kappa = \gamma = 0.45 = 10\kappa_*$.

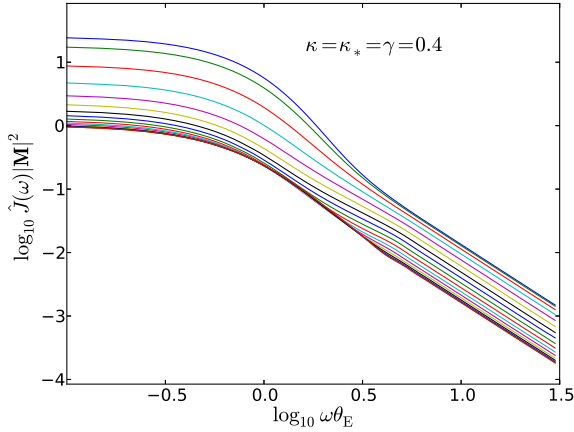


Figure 2. The numerically evaluated Fourier-transformed microlensing kernel $\hat{J}(\omega)$ for the macrolensing parameters of Image A in Q2237+0305 as given by Poindexter & Kochanek (2010). Constant along each curve is the angle (α) between the spatial wavevector ω and the major axis of the macrolensing matrix \mathbf{M} [eq. (1)], i.e., the eigenvector corresponding to the smaller eigenvalue, $1 - \kappa - \gamma$. These values are uniformly spaced from $\alpha = 0$ (top curve) to $\alpha = \pi/2$ (bottom).

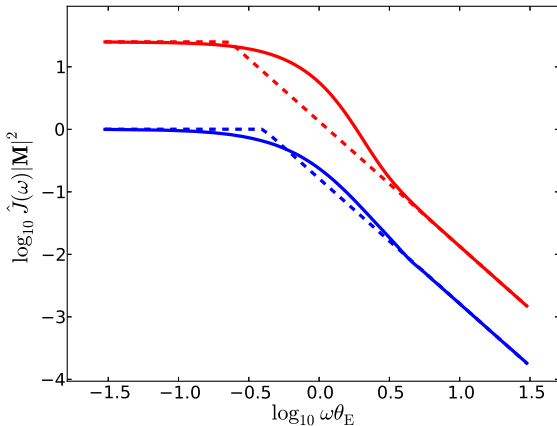


Figure 3. Solid lines are the extreme values $\alpha = 0$ (upper curve, in red) and $\alpha = \pi/2$ (lower, blue) from Fig. 2. Broken dashed lines show the asymptotic predictions (21).

4.1 Inhomogeneous disks

(Dexter & Agol 2011, hereafter DA)’s have proposed toy models of inhomogeneous disks, in which the disk temperature fluctuates around its steady-state value. These models are an interesting test of our formalism. They have more structure than simple gaussian source models, yet have spatial power spectra that are rather easily described. The fluctuations are spatially correlated within cells whose width is constant in azimuth and log radius. Each cell radiates as a black body at a temperature chosen from a log-normal distribution ($\log \equiv \log_{10}$):

$$\exp \left\{ \left[\log T_r - \log T_{r,0} + \sigma_T^2 \right]^2 / \sigma_T^2 \right\} \frac{d \log T_r}{\sqrt{\pi} \sigma_T}. \quad (22)$$

Here $T_{0,r} \propto (r/r_s)^{-3/4}$ is the temperature profile of a homogeneous disk with a constant mass accretion rate, neglecting the inner and outer edges. The fiducial radius is defined so that $T_{0,r} = h/k_B \lambda$ at $r = r_s$ if λ is the wavelength of observation referred to the disk rest frame. Following eq. (22), the variance of $\ln T_r$ is $(\sigma_T \ln 10)^2/2$, and the mean of $\ln T_r$ is less than $\ln T_{r,0}$. The bolometric flux is the same on average as for the homogeneous disk: $\langle T_r^4 \rangle = T_{0,r}^4$. The narrow-band luminosity, however, decreases with increasing temperature variance: $L_\lambda(\sigma_T) = L_\lambda(0) \exp[-\frac{8}{9}(\sigma_T \ln 10)^2]$. At the same time, the apparent size of the source increases: the n^{th} radial moment of the light scales $\propto L_\lambda r_s^n \exp[\frac{4}{9}n(n+1)(\sigma_T \ln 10)^2]$.

The fiducial radius scales with the black-hole mass and accretion rate as $r_s \propto (M\dot{M})^{1/3}$. However, without reference to M or \dot{M} , one can infer the half-light radius $r_h(0)$ of a homogeneous disk from the observed narrow-band luminosity, corrected for lensing: $r_h(0) \propto L_\lambda^{1/2} \lambda^{3/2}$. The constant of proportionality depends only on fundamental constants if point on the disk radiates as a black body with temperature scaling as $r^{-3/4}$.

Based on the temporal variability and optical-to-UV spectra of QSOs, as well as the microlensing observations, DA conclude that $0.35 \lesssim \sigma_T \lesssim 0.5$. Since, as they remark, $r_h(\sigma_T)/r_h(0) \propto \exp[0.85(\sigma_T \ln 10)^2]$, it follows that the half-light radii are larger than those of homogeneous disks by factors of 1.7 to 3 when referred to the same L_λ .

To apply our methods, we must estimate the spatial power spectra of these models. We take the disk to be viewed face on and adopt angular coordinates $\theta \equiv \mathbf{r}/D_S$ in the source plane; in particular, $\theta_s \equiv r_s/D_S$. Polar coordinates (θ, ϕ) are defined so that $\theta = (\theta \cos \phi, \theta \sin \phi)$. We numerically average the Planck function at each radius in the disk over the temperature distribution (22), thus obtaining the mean source $\langle I(\theta) \rangle_S$. This is axisymmetric, as is its Fourier/Hankel transform,

$$\langle \hat{I}(\omega) \rangle_S = 2\pi \int_0^\infty J_0(\omega\theta) \langle I(\theta) \rangle_S \theta d\theta. \quad (23)$$

The subscript S serves as a reminder that the average is taken over realizations of the source, not over the microlensing. The spatial correlation of the temperature fluctuations—the size of the cells—plays no role in eq. (23), because the average $\langle I(\theta) \rangle_S$ of the surface brightness is computed independently at each point on the disk.

Eq. (7) for the microlensing flux variance involves $|\hat{I}(\omega)|^2$. Since this is a random variable in DA’s inhomogeneous models, we must average it over realizations of the source:

$$\langle |\hat{I}(\omega)|^2 \rangle_S = |\langle \hat{I}(\omega) \rangle_S|^2 + \text{var}_S[\hat{I}(\omega)]. \quad (24)$$

The last term is the Fourier transform of the two-point correlation of the surface brightness fluctuations, $\langle \Delta I(\theta_1) \Delta I(\theta_2) \rangle$, which vanishes unless the points θ_1 and θ_2 belong to the same cell. The correlation depends on $\phi_1 - \phi_2$, $\ln(\theta_1/\theta_2)$, and $\ln \bar{\theta} \equiv \frac{1}{2} \ln(\theta_1 \theta_2)$, but varies more rapidly with the first two variables than the third if N_r , the number of cells per octave in radius, is large. Thus to an adequate approximation,

$$\langle \Delta I(\theta_1, \phi_1) \Delta I(\theta_2, \phi_2) \rangle_S \approx \text{var}[I(\theta_1)] W_\phi(\phi_1 - \phi_2) W_\theta(\ln \theta_1 - \ln \theta_2), \quad (25)$$

where W_ϕ and W_θ are triangular window functions of width $2\pi/N_\phi$ and $(\ln 2)/N_r$, respectively, N_ϕ being the number of cells in azimuth. Then¹

$$\text{var}_S[\hat{I}(\omega)] \approx \frac{(2\pi)^2 \ln 2}{N_\theta N_\phi} \sum_{n=-N_\phi/2}^{N_\phi/2-1} \int_0^\infty \text{var}_S[I(\theta)] J_n^2(\omega\theta) \times \text{sinc}^2\left(\frac{\omega\theta \ln 2}{2N_r}\right) \theta^3 d\theta. \quad (26)$$

The strength of this term relative to the first term on the right side of (24) increases with σ_T at fixed $N_\theta N_\phi$. DA state that they obtain the best match to the variability data if the number of cells per octave in radius is in the range $100 \lesssim n \lesssim 1500$. We interpret this n to correspond to $N_\theta N_\phi$ in our notation. DA do not specify the aspect ratio of their cells. We presume that they are roughly square, although because of differential rotation, one might expect that the correlation length of disk inhomogeneities should be longer in azimuth than in radius. We take $N_\theta = 10$, $N_\phi = 55$, so that $\Delta\theta = 0.11$ rad and $\Delta \ln r = 0.069$. We normalize the power spectra to unity at $\theta = 0$: $P(\omega) = \langle |\hat{I}(\theta)|^2 \rangle_S / \langle |\hat{I}(0)|^2 \rangle_S$. This is not the same as normalizing by the square of the mean flux, $\langle F \rangle_S = \langle \hat{I}(0) \rangle_S$. When microlensing is measured via flux ratios of macroimages, after correction for time delays, intrinsic variations of the source flux cancel. Normalizing the power spectrum to unity at $\theta = 0$ is therefore more appropriate than normalizing by the average flux. In practice, it does not much matter which normalization one uses for DA's preferred parameter range. The ratio $\langle \hat{I}(0)^2 \rangle_S / \langle \hat{I}(0) \rangle_S^2$ increases with σ_T and decreases with $N_\theta N_\phi$. It is less than 1.04 for $\sigma_T \leq 0.5$ at $N_\theta N_\phi = 550$, but rises rapidly for larger temperature dispersions, reaching 4.53 at $\sigma_T = 0.7$.

Figure 4 shows the source power spectra calculated as described for several values of σ_T . As expected, the general effect of increasing σ_T is to suppress the power spectrum at $\omega\theta_s \lesssim 2$, because the mean source size increases. However, at least for $\sigma_T \lesssim 0.5$, the power spectrum is actually enhanced at larger ω , probably because the hottest individual cells, which are much smaller than θ_s , increasingly dominate. Comparison of the solid and dashed curves shows that for $\sigma_T \lesssim 0.5$, the power spectrum is nearly equal to the square of the Fourier transform of the mean intensity, which is independent of cell size. For $\sigma_T \gtrsim 0.7$, however, the cell-to-cell variance is more important, so that the second term in eq. (24) cannot be neglected.

Figure 5 shows the microlensing variance calculated by applying eq. (7) to the power spectra shown in fig. (4). On the abscissa, the size of the source is measured not by θ_s , but rather by the half-light radius of a homogeneous disk of equivalent narrow-band luminosity: $\theta_h(0) = 2.44 \exp[-(4/9)(\sigma_T \ln 10)^2] \theta_s$. At fixed $\theta_h(0)$, larger σ_T makes for a larger true source size and therefore, as expected, smaller microlensing flux variations. To gauge the effect of the temperature fluctuations on the source size inferred from microlensing, it is more appropriate to consider

¹ The use of $\text{sinc } x \equiv (\sin x)/x$ is a further approximation but is accurate when $\omega\theta \gg \max(|n|, 1)$; in the opposite limit, the integrand is negligible anyway. For numerical quadratures we replace $\text{sinc}^2(x/2)$ with $\text{sech}^2(x/\pi)$, which has the same equivalent width and the same effect of suppressing the integrand where ω is larger than the reciprocal of the local cell size, but avoids the sidelobes.

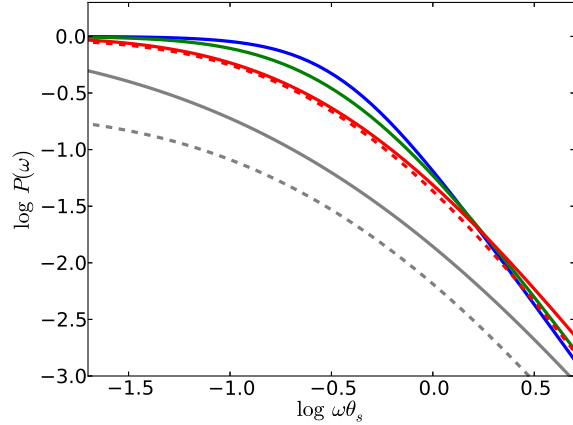


Figure 4. Spatial power spectra of inhomogeneous disks with log-normal temperature variations, following Dexter & Agol (2011). Power spectra are normalized to unity at wavenumber $\omega = 0$. Abscissa is scaled by the angular radius θ_s at which $hc/k_B T_{\text{eff}} = \lambda_{\text{rest}}$ in the homogeneous ($\sigma_T = 0$) disk. From top to bottom at $\log \omega\theta_s \approx -0.5$, solid curves correspond to $\sigma_T = \{0, 0.3, 0.5, 0.7\}$. Dashed curves show $\langle \hat{I}(\omega) \rangle_S^2 / \langle \hat{I}(0) \rangle_S^2$ rather than $P(\omega) \equiv \langle \hat{I}^2(\omega) \rangle_S / \langle \hat{I}^2(0) \rangle_S$ for the most variable cases ($\sigma_T = 0.5, 0.7$).

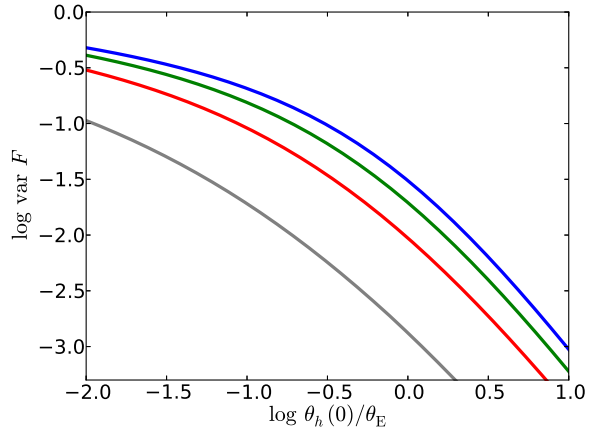


Figure 5. Microlensed flux variance of the inhomogeneous disks from Figure 4 for the fiducial microlensing parameters $\kappa = \gamma = 0.45$, $\kappa_* = 0.045$ versus inferred half-light radii $\theta_h(0)$ of homogeneous disks of the same L_λ . From top to bottom at $\log \theta_h(0)/\theta_E \approx -1$, the curves correspond to $\sigma_T = 0, 0.3, 0.5, 0.7$.

the horizontal rather than vertical distance between curves, i.e., the dependence of $\theta_h(0)$ on σ_T at fixed $\text{var } F$. For example, along the curve for $\sigma_T = 0$, variances of 0.05, 0.1, 0.2, and 0.4 are achieved for $\theta_h(0)/\theta_E = 0.649, 0.303, 0.106$, and 0.0191; whereas for $\sigma_T = 0.5$, these same variances require $\theta_h(0)/\theta_E = 0.212, 0.0879, 0.0266$, and 0.00421. The former sizes are larger than the latter by factors ranging from 3.1 to 4.5: these are the factors by which the size of a $\sigma_T = 0.5$ source inferred from microlensing variability would exceed the size inferred by fitting a conventional disk to its narrow-band luminosity. If one plots the microlensing vari-

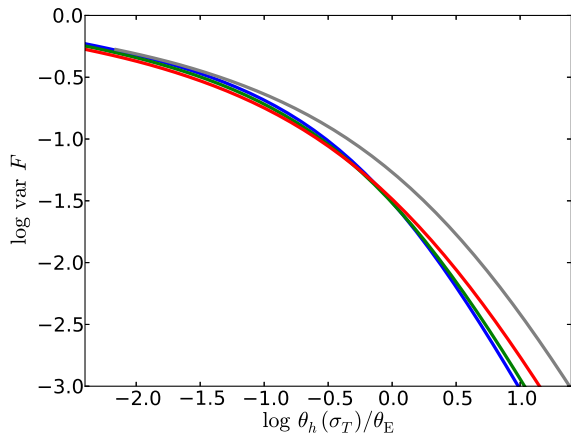


Figure 6. Like Fig. 5, but plotted against the true half-light radius of the mean inhomogeneous source. From top to bottom at $\log \theta_h(\sigma_T)/\theta_E \approx +1$, the curves correspond to $\sigma_T = 0.7, 0.5, 0.3, 0$.

ance against the *true* half-light radius of the corresponding mean source, then the curves lie almost on top of each other, at least for $\theta_h \lesssim \theta_E$ (Fig. 6). This confirms the common wisdom that microlensing variability is relatively insensitive to the details of the source structure at a given half-light radius. However, this rule of thumb breaks down for sufficiently wild sources, as the curve for $\sigma_T = 0.7$ shows.

4.2 Comparison with simulations

We have tested the predicted flux variance against simulations carried out with an elementary inverse-ray-shooting code. The code is our own but its design follows Kochanek (2004). The source and lens plane are taken to be periodic, with periodicity lengths in the ratio $L_x/L_y = 1$ on the source plane and $(1-\kappa+\gamma)/(1-\kappa-\gamma)$ on the lens plane. All simulations reported here were performed for $\kappa = \gamma = 10\kappa_* = 0.45$, so $(L_x/L_y)_{\text{imageplane}} \rightarrow 10$. Lensing stars having a log-normal distribution of masses ($\sigma_{\text{mass}} = 0.3$ dex) are scattered over the lens plane with mean number density $\kappa_*/\pi\theta_E^2$. Their masses are assigned to grid points using a cloud-in-cell method, and the deflections they cause are computed by Fourier transforms using a particle-mesh (PM) method.² The numbers of cells along each dimension of lens domain are in the ratio $N_x/N_y \approx \sqrt{L_x/L_y} \rightarrow \sqrt{10}$, on the theory that because of the macrolensing shear, the four microimages³ split by an isolated on-axis star have separations along x and y that lie in this ratio. The rays form a uniform mesh in the image plane with four rays per grid cell, corresponding to $4\sqrt{10}$ per (square) cell in the source plane, for a total

² Kochanek (2004) used P³M to better resolve short-range forces. However, we typically have $\lesssim 10^{-4}$ stars per grid point. Hence the few rays that pass within a cell width of a star carry little light (all rays being weighted equally). They contribute even less to caustics because large deflections entail strong demagnification.

³ The softened potentials of our simulated stars create an odd number of images, but the central image is demagnified.

of 3.4×10^8 rays in our largest simulations. It has been argued that a much larger number of rays per cell is needed for accurate results with the inverse-ray-shooting method (e.g. Mediavilla et al. 2006). However, that conclusion is reached on the basis of a pixel-by-pixel comparison with some analytic solution such as that for an isolated star. We smooth the source-plane magnification pattern with Gaussians before computing the flux variance, so it is the number of rays per smoothing length or the number per star that is relevant.

Table 4.2 compares the variances obtained from our simulations to the semi-analytic predictions for Gaussian sources⁴ with dispersions ranging from $\sigma_S = 0.005\theta_E$ to $0.08\theta_E$. The first column lists the periodicity length in the y direction, which is common to the source and lens/image planes; $L_x = L_y$ in the source plane and $= 10L_y$ in the image plane. The second and third columns give the number of grid points in each dimension, and the fourth, the number of stars. In columns 5–9, the numbers in parentheses represent the uncertainty in the last digit of the estimated variance based on the spread in the results of four simulations sharing the same parameters listed in the first four columns but differing in the random assignments of positions and masses to the stars.

The flux variances estimated from the simulations are clearly noisy, but the agreement with theory tends to improve both with resolution and with domain size. The improvement with domain size is in part merely a reduction in noise due to the larger numbers of stars, but there appears also to be a systematic trend in the mean values, which suggests that long-range forces are important. In a periodic domain, the forces exerted by each star must also be periodic and hence cannot follow the correct scaling $\phi \propto |\Delta\theta|^{-1}$ at separations $\Delta\theta$ larger than about half the periodicity length. We have found that the variances are sensitive to the approximation chosen for the force kernel. The results shown here were obtained by constructing the force kernel in coordinate space and windowing the exact kernels for the x and y components of the deflection with $\cos(\pi\Delta\theta_x/L_x)$ and $\cos(\pi\Delta\theta_y/L_y)$, respectively. More sophisticated simulation algorithms, such as the inverse-polygon method of Mediavilla et al. (2006), would likely improve the rate of convergence with resolution. It would be interesting to see whether they also help the convergence with domain size.

5 SUMMARY

Motivated in part by discrepancies between the angular sizes of QSOs inferred from microlensing and those expected from disk theory, we have developed a practical method for computing the variance of the microlensed fluxes of angularly extended sources of arbitrary structure. The method requires as inputs the spatial power spectrum of the unlensed source, the shear and convergence provided by the smooth mass distribution of the lensing galaxy, and the mean number density and mass function of the lensing stars. We have written and made available for download a small suite of codes that accepts these inputs and calculates the microlensing variance. The mathematical formulation of the method is described

⁴ I.e., the unlensed surface brightness is $I_0(\theta) \propto \exp(-\theta^2/2\sigma_S^2)$.

Table 1. Microlensed flux variances of gaussian sources from simulations and the semianalytic method. Lensing parameters $\kappa = \gamma = 0.45$, $\kappa_* = 0.045$, & $\sigma_{\text{mass}} = 0.30$ dex. See text for column headings.

L_y [θ_E]	N_x	N_y	N_*	$\sigma_S =$	0.005 θ_E	0.01 θ_E	0.02 θ_E	0.04 θ_E	0.08 θ_E
<i>Resolution tests</i>									
51.2	8192	2592	477	0.56(1)	0.48(1)	0.40(1)	0.32(1)	0.236(6)
51.2	16384	5184	477	0.63(2)	0.55(2)	0.46(1)	0.37(1)	0.28(1)
<i>Domain-size tests</i>									
25.6	4096	1296	119	0.58(3)	0.50(2)	0.42(2)	0.33(2)	0.25(2)
51.2	8192	2592	477	0.56(1)	0.48(1)	0.40(1)	0.32(1)	0.236(6)
102.4	16384	5184	1907	0.602(7)	0.525(7)	0.440(6)	0.353(6)	0.267(5)
Semi-analytic					0.6134	0.5286	0.4440	0.3598	0.2767

above in sufficient detail to allow an interested user to understand the workings of our codes. Further improvements in efficiency and accuracy are doubtless possible. The semi-analytic method has been tested against a simple inverse-ray-shooting simulation code and compared with the published results of Dexter & Agol (2011) for their toy models of highly inhomogeneous disks.

Perhaps the most important lesson learned from these tests is that significant numerical effort—in terms of the numbers of pixels and simulated stars, as well as the number of independent trials—is necessary to obtain good agreement between the flux variance estimated from the simulations and that calculated semi-analytically by the method developed here. Doubtless a cleverer simulation method could get by with fewer rays, but the need to simulate a large region of the lens planes, $\gtrsim 10^2 \theta_E$ on a side, seems inescapable, at least when the macrolensing magnification is large (~ 10), as it typically is in present lensing surveys.

ACKNOWLEDGMENTS

We thank Jason Dexter for help with understanding Dexter & Agol (2011).

REFERENCES

Abramowitz M., Stegun I. A., 1970, Handbook of mathematical functions : with formulas, graphs, and mathematical tables. U.S. Government Printing Office
 Anguita T., Schmidt R. W., Turner E. L., Wambsganss J., Webster R. L., Loomis K. A., Long D., McMillan R., 2008, A&A, 480, 327
 Armitage P. J., Natarajan P., 2002, ApJ, 567, L9
 Bate N. F., Floyd D. J. E., Webster R. L., Wyithe J. S. B., 2008, MNRAS, 391, 1955
 Blackburne J. A., Pooley D., Rappaport S., Schechter P. L., 2011, ApJ, 729, 34
 Brouwer D., Clemence G. M., 1961, Methods of celestial mechanics. New York: Academic Press
 Chabrier G., 2003, PASP, 115, 763
 Chandrasekhar S., 1943, Reviews of Modern Physics, 15, 1

Deguchi S., Watson W. D., 1987, Physical Review Letters, 59, 2814
 Dexter J., Agol E., 2011, ApJ, 727, L24
 Eigenbrod A., Courbin F., Meylan G., Agol E., Anguita T., Schmidt R. W., Wambsganss J., 2008, A&A, 490, 933
 Floyd D. J. E., Bate N. F., Webster R. L., 2009, MNRAS, 398, 233
 Goodman J., Tan J. C., 2004, ApJ, 608, 108
 Hardy G. H., 1949, Divergent Series. Clarendon Press
 Jiménez-Vicente J., Mediavilla E., Muñoz J. A., Kochanek C. S., 2012, ApJ, 751, 106
 Kochanek C. S., 2004, ApJ, 605, 58
 Kundic T., Wambsganss J., 1993, ApJ, 404, 455
 Lightman A. P., Eardley D. M., 1974, ApJ, 187, L1
 Mediavilla E., Muñoz J. A., Falco E., Motta V., Guerras E., Canovas H., Jean C., Oscoz A., Mosquera A. M., 2009, ApJ, 706, 1451
 Mediavilla E., Muñoz J. A., Lopez P., Mediavilla T., Abajas C., Gonzalez-Morcillo C., Gil-Merino R., 2006, ApJ, 653, 942
 Miralda-Escudé J., 1991, ApJ, 370, 1
 Morgan C. W., Kochanek C. S., Morgan N. D., Falco E. E., 2010, ApJ, 712, 1129
 Mosquera A. M., Muñoz J. A., Mediavilla E., Kochanek C. S., 2011, ApJ, 728, 145
 Muñoz J. A., Mediavilla E., Kochanek C. S., Falco E. E., Mosquera A. M., 2011, ApJ, 742, 67
 Neindorf B., 2003, A&A, 404, 83
 Poindexter S., Kochanek C. S., 2010, ApJ, 712, 658
 Poindexter S., Morgan N., Kochanek C. S., 2008, ApJ, 673, 34
 Pooley D., Blackburne J. A., Rappaport S., Schechter P. L., 2007, ApJ, 661, 19
 Pringle J. E., 1996, MNRAS, 281, 357
 Rauch K. P., Blandford R. D., 1991, ApJ, 381, L39
 Seitz C., Schneider P., 1994, A&A, 288, 1
 Seitz C., Wambsganss J., Schneider P., 1994, A&A, 288, 19
 Syunyaev R. A., Shakura N. I., 1975, Soviet Astronomy Letters, 1, 158
 Wyithe J. S. B., Webster R. L., Turner E. L., 2000, MNRAS, 312, 843
 Young P., 1981, ApJ, 244, 756